

Tuning the Surface Chemistry of MXene to Improve Energy Storage: Example of Nitrification by Salt Melt

Liyuan Liu, Hannes Zschiesche, Markus Antonietti,* Barbara Daffos, Nadezda V. Tarakina, Mathieu Gibilaro, Pierre Chamelot, Laurent Massot, Benjamin Duployer, Pierre-Louis Taberna, and Patrice Simon*

The unique properties of 2D MXenes, such as metal-like electrical conductivity and versatile surface chemistry, make them appealing for various applications, including energy storage. While surface terminations of 2D MXene are expected to have a key influence on their electrochemical properties, the conventional HF-etching method limits the surface functional groups to $-F$, $-OH$, and $-O$. In this study, O-free, Cl-terminated MXenes (noted as $Ti_3C_2Cl_x$) are first synthesized by a molten salt ($FeCl_2$) etching route. Then, a substitution of surface termination from Cl- to N- is performed via post-thermal treatment of $Ti_3C_2Cl_x$ in Li_3N containing molten salt electrolytes. While the Cl-terminated pristine material does not show electrochemical activity, the surface-modified, N-containing $Ti_3C_2T_x$ exhibits a unique capacitive-like electrochemical signature in sulfuric acid aqueous electrolyte with rate performance—more than 300 F g^{-1} (84 mAh g^{-1}) at 2 V s^{-1} . These results show that control of the MXene surface chemistry enables the preparation of high-performance electrodes in a previously not accessed limit of energy storage.

1. Introduction

Since their discovery in 2011, 2D transition metal carbides or carbonitrides (MXenes)^[1,2] became a focal point of nanomaterials, notably for electrochemical energy storage.^[3–6] The general formula of MXene is $M_{n+1}X_nT_x$ ($n = 1–3$), where M represents an early transition metal, X is carbon and/or nitrogen, and T_x stands for the surface groups originating from the etchant^[3] and the need for charge neutrality. In the past 10 years, aqueous solutions containing fluoride ions (HF ,^[2] $LiF+HCl$ ^[4]) remained the mainstream etching agent for the parental MAX phase, which naturally leads to mainly $-F$, $-OH$, and $-O$ surface terminated MXenes (noted HF-MXenes). By performing DFT simulations or first-principles calculations,

many research groups already reported that the surface functional groups are the main factor affecting the electronic characteristics of MXene materials and, consequently, their electrochemical performance.^[7–10] Experimental studies also observed the significant influence of MXene surface terminations on the electrochemical properties of MXene electrodes by performing chemical or thermal surface modifications.^[11,12] For example, Dall'Agnese et al. replaced $-F$ with $-O$ surface groups by chemical treatment in alkaline electrolytes, obtaining a four-fold increase of the capacitance in sulfuric acid electrolytes.^[13] The conventional HF-etching experimental method used to prepare MXene simply limits the variety of surface functional groups, and this is why most of the studies on tuning the surface terminations of MXene are based on theoretical predictions.^[7–10] Moreover, the use of hazardous HF or F-containing acid electrolytes brings safety concerns and limits the potential broader application. In this context, it is important to find an eco-friendly and safe alternative etching route allowing for tuning the surface termination of MXenes.

In 2019, Li et al. reported a new Lewis-acidic molten salt method to prepare surface F-free, Cl-terminated MXenes by reacting the MAX phase in molten $ZnCl_2$.^[14] Together with the authors of this pioneering work, we have extended this molten salt synthesis route as a general approach to producing MXenes (noted as MS-MXenes) by playing with a wide range of elements for A-site of the MAX phase (Zn, Al, Si, Ga) and salt melt composition.^[15] As a result, not only Cl, but Br and I-terminated MXenes

L. Liu, B. Daffos, B. Duployer, P.-L. Taberna, P. Simon
CIRIMAT

UMR CNRS 5085

Toulouse III - Paul Sabatier University

118 route de Narbonne, 31062 Toulouse, France

E-mail: patrice.simon@univ-tlse3.fr

L. Liu, B. Daffos, B. Duployer, P.-L. Taberna, P. Simon
RS2E

French Research Network on Electrochemical Energy Storage

FR CNRS 3459, 80039 Amiens Cedex, France

H. Zschiesche, M. Antonietti, N. V. Tarakina

Max Planck Institute of Colloids and Interfaces

Research Campus Golm

D-14476 Potsdam, Germany

E-mail: markus.antonietti@mpikg.mpg.de

M. Gibilaro, P. Chamelot, L. Massot

Chemical Engineering Laboratory - LGC

Toulouse III - Paul Sabatier University

UPS-CNRS-INPT

118 Route de Narbonne, 31062 Toulouse Cedex 09, France



The ORCID identification number(s) for the author(s) of this article can be found under <https://doi.org/10.1002/aenm.202202709>.

© 2022 The Authors. Advanced Energy Materials published by Wiley-VCH GmbH. This is an open access article under the terms of the Creative Commons Attribution-NonCommercial-NoDerivs License, which permits use and distribution in any medium, provided the original work is properly cited, the use is non-commercial and no modifications or adaptations are made.

DOI: 10.1002/aenm.202202709

were successfully prepared. Meanwhile, O surface terminations were unavoidable introduced by the washing step in ammonium persulfate (APS) needed to remove metallic impurities. Interestingly, Cl- and O-terminated MXenes after APS washing already achieved high performance as a negative electrode for Li-ion intercalation in non-aqueous electrolytes. However, in contrast to HF-MXene, the Cl- and O-terminated MS-MXenes behaves very poorly in the aqueous electrolyte. In 2021, the hybrids of Ti_3C_2 and Cu and/or Co prepared via molten salt etching were used as electrode material for an aqueous supercapacitor.^[16] In these experiments, a pair of sharp redox peaks with big cathodic and anodic peak potential separation (>200 mV at 50 mV s^{-1}) was observed in the cyclic voltammetry (CV) profile, indicating a comparably sluggish electrochemical reaction kinetics of MS-MXenes in aqueous electrolytes. The bottom line here is that similar to heterogeneous catalysis, surface termination groups are the main driver optimizing the charge transfer to the material. In the same year, Kamysbayev et al. further enriched the types of surface termination of MXene by substitution of Cl and Br surface terminations with O, NH, S, Se, and Te.^[17] However, all these reactions were performed in an Ar-filled glove box with

oxygen and moisture levels below 1 ppm, which makes synthesis restricted to specially installed laboratories.

In the present study, O-free, Cl-terminated MXenes (noted as $\text{Ti}_3\text{C}_2\text{Cl}_x$) were synthesized by the molten salts (FeCl_2) etching route by replacing the oxidative chemical washing step in APS with a physical magnet cleaning method. Then, surface termination was changed from Cl- to N- (with minor O-) via a second thermal treatment of $\text{Ti}_3\text{C}_2\text{Cl}_x$ in Li_3N (termed N-containing $\text{Ti}_3\text{C}_2\text{T}_x$). The surface-modified N-containing $\text{Ti}_3\text{C}_2\text{T}_x$ exhibits a unique electrochemical signature in sulfuric acid aqueous electrolytes at very high rates (303 F g^{-1} at 2 V s^{-1}), a capacitive-like redox process within the full voltage window of 1.0 V. Taking these values into a structure model we can learn that these described record values of supercapacitance are close to the Langmuir monolayer limit where energy storage is not controlled by electron-electron repulsion within the material, but by the dense packing of counterions on its surface. Beyond that, we further performed in situ XRD techniques to clarify the charge storage mechanism. These results show that tuning the surface chemistry in MXene brings new chemical options to design high-rate redox capacitive materials for the next generation of high-power storage devices.

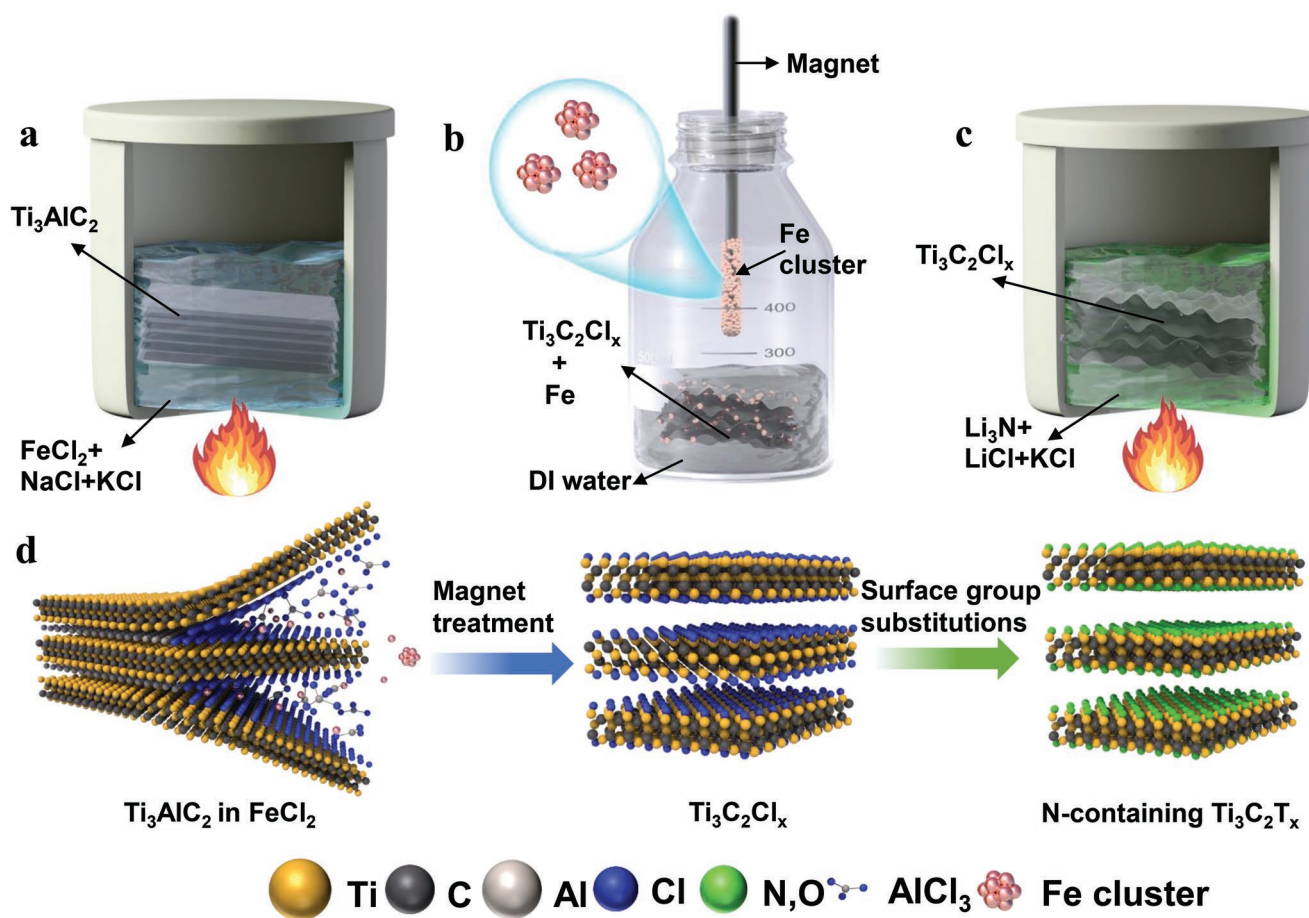
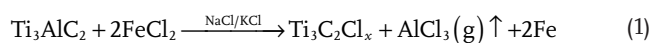


Figure 1. Schematic illustration of the fabrication process of N-containing $\text{Ti}_3\text{C}_2\text{T}_x$. a) Ti_3AlC_2 MAX is immersed in $\text{NaCl}+\text{KCl}$ molten salt containing the Lewis acidic FeCl_2 during annealing in an Ar furnace. b) The MXene products achieved right after FeCl_2 etching are dissolved in a water solution. Insoluble Fe-containing by-products are removed by a magnet to achieve pure $\text{Ti}_3\text{C}_2\text{Cl}_x$ MXene. c) $\text{Ti}_3\text{C}_2\text{Cl}_x$ MXene is immersed in $\text{LiCl}+\text{KCl}$ molten salt containing the Li_3N during annealing in an Ar furnace. d) The redox coupling reaction between Ti_3AlC_2 and dissolved FeCl_2 leads to the formation of $\text{Ti}_3\text{C}_2\text{Cl}_x$ MXene and Fe, analogous to our previous work.^[15] N-containing $\text{Ti}_3\text{C}_2\text{T}_x$ is obtained after surface group substitution in Li_3N .

2. Results and Discussion

2.1. Synthesis of MS-MXene with Various Surface Terminations

Figure 1 shows a sketch of the $\text{Ti}_3\text{C}_2\text{T}_x$ MXene preparation. It starts from the Ti_3AlC_2 MAX phase etching by FeCl_2 (Figure 1a), followed by magnetic separation of Fe impurity and (Figure 1b) surface termination substitution in Li_3N (Figure 1c). More specifically, the molten salt etching consists of a reaction between Ti_3AlC_2 and FeCl_2 at 700 °C (Equation (1)). Once reaching a molten state, the Al layer in Ti_3AlC_2 started to be oxidized into Al^{3+} by concomitant reduction of the Fe^{2+} into metallic Fe, leading to the generation of the aluminum halide gas AlCl_3 (Figure 1d). The excess Fe^{2+} can oxidize the outmost Ti atoms of Ti_3C_2 , and halogen ions finally functionalize the MXenes by charge compensation (Equation (1)).



After washing with H_2O to dissolve the residual salts, two different treatments were used to remove the Fe-based impurities. First, a magnet was placed in the solution during MXene washing with H_2O , leading to iron-containing by-products removal from the MXene—"magnetic separation"—without the need for any further oxidative chemical treatment (Figure 1b; Figure S1, Supporting Information). Alternatively, the conventional oxidative APS washing step was performed

for comparison. The magnetic separation method allows for preparing mainly Cl-terminated $\text{Ti}_3\text{C}_2\text{Cl}_x$, while APS washing results in the addition of O-containing functional groups (noted as $\text{Ti}_3\text{C}_2\text{Cl}_x\text{O}_y$), as a result of surface oxidation.^[15] In a second step, a surface termination exchange reaction of magnet-treated $\text{Ti}_3\text{C}_2\text{Cl}_x$ was performed by substituting Cl with N-terminations through immersion in a molten salt electrolyte containing the strong nucleophile Li_3N dissolved in LiCl/KCl (Figure 1d and Equation (2)).



This is also thermodynamically feasible as the binding energy of Ti–Cl ($405 \pm 11 \text{ kJ mol}^{-1}$)^[18] (see Table S1, Supporting Information) is known to be lower than Ti–F ($569 \pm 33 \text{ kJ mol}^{-1}$) and Ti–O ($672 \pm 9 \text{ kJ mol}^{-1}$) bonds in HF-MXenes.

2.2. Material Characterization of Cl-Containing $\text{Ti}_3\text{C}_2\text{T}_x$

Figure 2a shows the XRD patterns of the pristine Ti_3AlC_2 MAX precursor before and after etching by FeCl_2 , followed by magnetic separation or APS washing to remove Fe. Compared to the pristine Ti_3AlC_2 , most of the diffraction peaks disappeared right after FeCl_2 molten salt etching, while the shift of intense (002) peak from 9.6° to 8.0° indicates an expansion of the interlayer distance from 9.2 to 11.1 Å. The sharp peaks located at 45.5° and

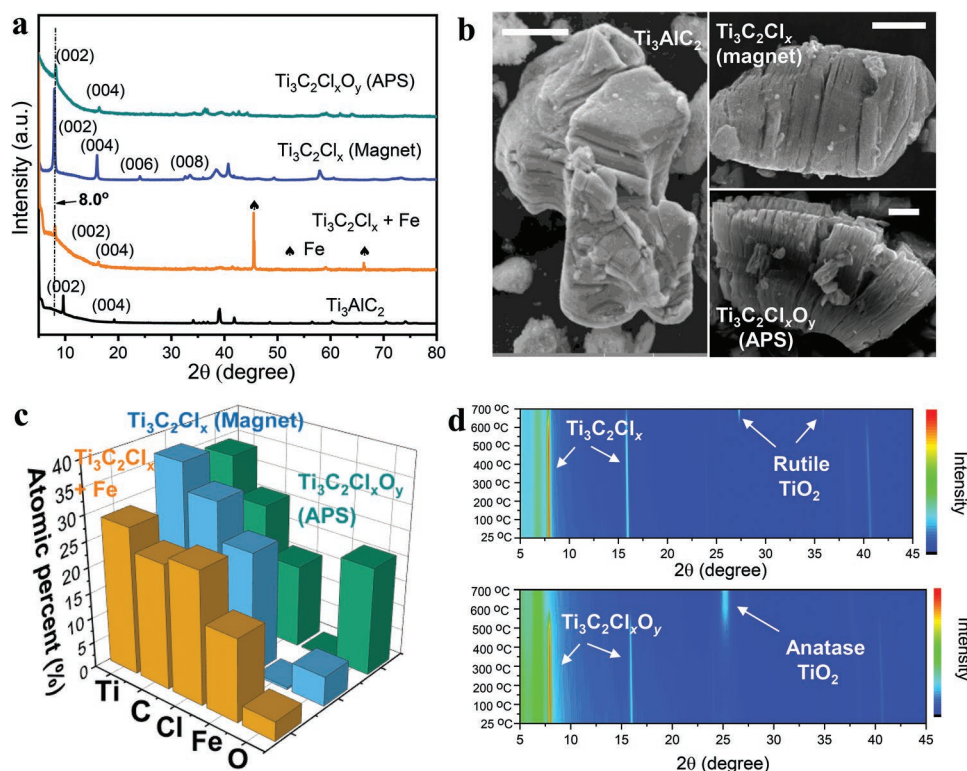


Figure 2. Material characterization of Cl-terminated $\text{Ti}_3\text{C}_2\text{T}_x$ treated by magnetic separation or APS washing. a) XRD patterns of pristine Ti_3AlC_2 before (black line) and after reaction with FeCl_2 (orange line) followed by magnetic separation (blue line), and after washing in oxidative 0.1 M $(\text{NH}_4)_2\text{S}_2\text{O}_8$ (APS) solution (green line). b) SEM images of Ti_3AlC_2 , FeCl_2 etched $\text{Ti}_3\text{C}_2\text{T}_x$ treated by magnetic separation and APS washing (scale bar in the image is 2 μm). c) Comparison of elemental composition (at%) of FeCl_2 etched $\text{Ti}_3\text{C}_2\text{T}_x$ before and after treatment by magnet and APS solution by EDS analysis. d) In situ high-temperature XRD of FeCl_2 etched $\text{Ti}_3\text{C}_2\text{T}_x$ treated by magnet and APS.

66.3° can be indexed as metallic Fe, which disappeared after further magnetic separation, or direct APS washing, demonstrating that both processes are equally efficient to remove Fe. The removal of Fe, after “magnetic treatment,” is further confirmed by energy-dispersive spectroscopy (EDS) analysis (Figure S2, Supporting Information), where the Fe amount drops down to less than 1.0 at% after magnetic separation. Figure 2b compares the morphology of FeCl₂-etched Ti₃C₂T_x after magnetic separation or APS washing: the FeCl₂-etched Ti₃C₂T_x after magnetic separation exhibits a stacked multi-layered structure while the APS treated sample swells into a few-layered accordion-like morphology, which points to irregular surface oxidation of the MXene (Table S2, Supporting Information), as it can be expected after APS treatment. The semi-quantitative EDS analyses (Figure 2c; Table S3, Supporting Information) show Ti:Cl atomic ratios close to 3:1.88 after magnet separation, indicating that the surface termination group is almost exclusively Cl. After APS washing, the Cl content significantly decreases while O content largely increases. As a result, the atomic ratio of Ti:Cl drops down to less than 3:1.26, which quantifies the partial exchange of Cl with oxygen-containing functional groups. The modification of the MXene surface chemistry was further confirmed by water contact angle measurement (WCA). The WCA values are 81° and 56° (Figure S3, Supporting Information), respectively, for the magnet and APS-treated samples. This is in line with a higher oxygen content of the APS-treated sample, increasing the surface hydrophilicity.^[19] Those two findings support that the APS treatment introduces oxygen-containing polar groups resulting in the preparation of mixed Cl- and O-terminated Ti₃C₂Cl_xO_y MXene. Moreover, previously published temperature programmed desorption-mass spectrometry (TPD-MS) analysis showed a release of CO₂ with APS treated MXene, which was not observed for HF-Ti₃C₂T_x, further evidencing that the increase of O-content is due to partial MXene surface oxidation instead of removal of confined water.^[15]

Interestingly, as observed in Figure 2d and Figure S4, Supporting Information, the magnet-treated Ti₃C₂T_x (Ti₃C₂Cl_x) exhibits higher thermal stability than the APS-treated (Ti₃C₂Cl_xO_y) one. In situ XRD experiments have been performed at different temperatures—from room temperature to 700 °C—under N₂: the structure of magnet-treated MXene is well preserved up to 700 °C, even though a small amount of Rutile TiO₂ can be observed at 700 °C. Differently, the oxidation of APS-treated MXene starts at 400 °C, and the structure is destroyed from 500 °C, followed by the transformation into Anatase TiO₂. The above result evidences that magnet-treated Ti₃C₂T_x MXene has better oxidation stability or nobility than the APS-treated one, which could be linked to the absence of oxygen-containing functional groups.^[20] According to those results, we can assume that magnet-treated MXene is very poor in terminal oxygen groups, oppositely to APS-treated MXene.

2.3. Material Characterization of N-Containing Ti₃C₂T_x

The magnet-treated MXene Ti₃C₂Cl_x with improved thermal stability was selected for further surface termination exchange

via a second thermal treatment (Equation (2)) to prevent TiO₂ formation. Nitrogen surface termination groups were introduced by adding controlled amounts of Li₃N to the Ti₃C₂Cl_x powder in LiCl + KCl molten salt and heated at 550 °C for 12 h. After Li₃N treatment, the SEM image in Figure 3a shows that the stacked multi-layered structure is slightly expanded into a stack of many thin slices closely connected to each other, resulting in a few-layered, accordion-like morphology. Notably, the XRD patterns in Figure 3b show clear shifts of the (00l) peaks after Li₃N treatment, suggesting homogeneous surface group metathesis over all layers. Moreover, a shift of (002) diffraction peak from 2θ 8.0° to 7.0° reveals a systematic expansion of the interlayer distance from 11.0 to 12.5 Å. The EDS spectra in Figure S5, Supporting Information, clearly show the disappearance of the large Cl peak from pristine Ti₃C₂Cl_x after Li₃N-based post-thermal treatment, while the content of N element significantly increased. Combined CHNOS with ICP elemental analysis (Table S4, Supporting Information), the final composition of the N-containing Ti₃C₂T_x sample is Ti₃C_{1.95}N_{0.80}O_{1.11}H_{0.46}. Li₃N precursor can easily react with moisture and air thus bringing O-containing functional groups.^[21]

According to Fourier-transform infrared (FTIR) spectroscopy analysis (Figure 3c), the pristine Ti₃C₂Cl_x MXene only shows a broad spectral feature below 920 cm⁻¹, which could result from a convolution of C–Cl (850–550 cm⁻¹) vibrations and the Ti–C stretch (672 cm⁻¹).^[22] In contrast, the APS-treated Ti₃C₂Cl_xO_y sample (Figure S6, Supporting Information) exhibits two broad spectral features, the one below 726 cm⁻¹ can be assigned to the vibration of Ti–O (544 cm⁻¹)^[23] and Ti–C (672 cm⁻¹)^[24] while the other at 1633 cm⁻¹ comes from C=O, which is consistent with the TPD-MS results showing the formation of CO₂ gas.^[15] Differently, the spectra of N-containing Ti₃C₂T_x exhibits an initial broad peak below 619 cm⁻¹, which is attributed to the Ti–O (544 cm⁻¹)^[23] and Ti–C (672 cm⁻¹)^[24] stretching vibration modes. The following broad peak between 617 and 1274 cm⁻¹ could result from a convolution of Ti–N (957 cm⁻¹)^[25] vibrations, C–Ti–N and O–Ti–N stretch (1060 and 1205 cm⁻¹).^[22,26] The existence of C=N and C=C=N groups^[27] was validated by the presence of transmittance peaks at around 1635 and 2083 cm⁻¹, respectively. The broad features centered at ≈3622 cm⁻¹ evidence the presence of hydroxyl O–H or N–H stretch.^[23]

High-resolution transmission electron microscopy (HRTEM) and scanning (S)TEM combined with electron energy-loss spectroscopy (STEM-EELS) have been performed to identify the local environment (coordination), electronic structure, and valence state configuration by focusing on the Ti–L_{2,3}, Cl–L_{2,3} N–K, and C–K edges at the atomic scale. The two spectra of Cl- and N-containing Ti₃C₂T_x as shown in Figure 3d evidence the similar electronic structure of the MXene's Ti₃C₂ skeleton with three main peaks including C–K, Ti L_{2,3}, and O–K edges at the similar positions (approximate peak maximum) of ≈294, ≈456, ≈462, and ≈531 eV energy loss, respectively. The overall decrease in the Cl L_{2,3}-edge intensity directly reflects an almost negligible remaining amount of Cl in the N-containing Ti₃C₂T_x. Together with the FT-IR results, the presence of N–K edge signal at ≈398 eV supports the successful replacement of Cl-termination with N to prepare N-containing Ti₃C₂T_x MXene. In contrast, the fine structure at the Ti L_{2,3} edges (Figure S7c, Supporting Information) remain unchanged,

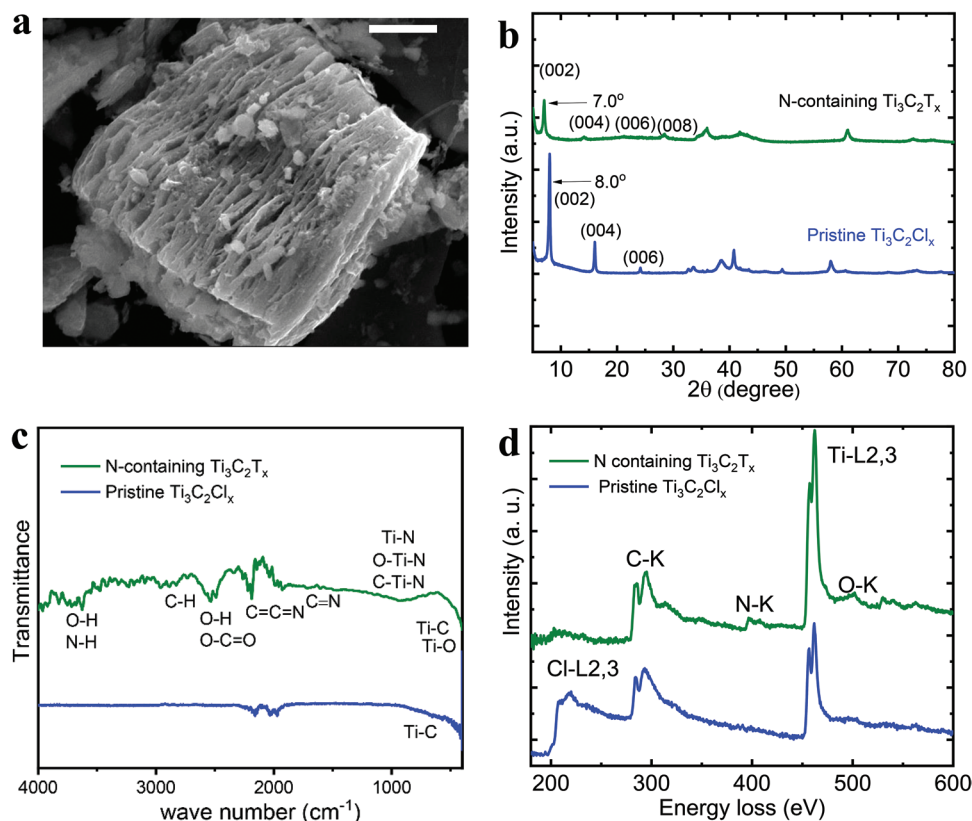


Figure 3. Material characterization of $\text{Ti}_3\text{C}_2\text{Cl}_x$ before and after surface termination substitution with N-containing groups. a) SEM images (scale bar in the image is 2 μm) of N-containing $\text{Ti}_3\text{C}_2\text{T}_x$; b) the XRD patterns, c) the FTIR patterns and d) electron energy-loss spectroscopy (EELS) analysis of magnet-treated pristine $\text{Ti}_3\text{C}_2\text{Cl}_x$ and N-containing $\text{Ti}_3\text{C}_2\text{T}_x$.

as no significant shifts of edges or changes in the L3/L2 ratio (0.76) were observed, indicating a similar titanium valence charge. The C–K, N–K, O–K, and Cl–L edges are determined by the hybridizations of these atoms with the Ti d bands, and the fine structure at the C–K edge is reported to be sensitive to the chemical nature and the location of the functional groups on the MXene's surface.^[28] Hence it appears that Cl and N T-groups have a similar influence on the electronic structure of the Ti_3C_2 -part of MXene based on their similar position and shape of the C–K edge (Figure S7d, Supporting Information). To understand their change on physical morphologies, $\text{Ti}_3\text{C}_2\text{Cl}_x$ and N-containing $\text{Ti}_3\text{C}_2\text{T}_x$ were further investigated by N_2 adsorption–desorption analysis to evaluate their specific surface area, porous volume, and pore size distribution. Figure S8, Supporting Information, shows that both samples show similar specific surface areas (21.0 and 21.3 $\text{m}^2 \text{g}^{-1}$, respectively for $\text{Ti}_3\text{C}_2\text{Cl}_x$ and N-containing $\text{Ti}_3\text{C}_2\text{T}_x$) and total porous volume (0.065 and 0.071 $\text{cm}^3 \text{g}^{-1}$). Those values are consistent with other results from the literature,^[29,30] revealing that the improvement on electrochemical performance of N-containing $\text{Ti}_3\text{C}_2\text{T}_x$ is mainly attributed to the modification of surface group instead of the increase of the surface area and porosity.

HR-STEM was further performed to achieve the atomically resolved structure of a thin edge from Cl- and N-containing $\text{Ti}_3\text{C}_2\text{T}_x$. High-resolution TEM images (Figure 4a,b) show both Cl- and N-containing $\text{Ti}_3\text{C}_2\text{T}_x$ contain many layers while the Cl-contained one has more compact and dense layers than the

N-containing $\text{Ti}_3\text{C}_2\text{T}_x$, which corresponds well to the previous SEM images. Layers of ordered $\text{Ti}_3\text{C}_2\text{T}_x$ MXene are resolved in a cross-sectional view along basal planes in Figure 4c,d and even atomic columns are resolved when imaging approximately along zone-axis orientation (Figure 4e,f). The periodicity in the out-of-basal plane direction matches well with their intense (00l) peaks in the XRD patterns. For each Cl-containing $\text{Ti}_3\text{C}_2\text{T}_x$ MXene layer (Figure 4e), up to five bright atomic planes can be identified per $\text{Ti}_3\text{C}_2\text{T}_x$ MXene layer. This bright contrast is directly interpretable as a mass (atomic number)-thickness contrast,^[31,32] the inner bright planes can be related to atomic planes occupied by Ti and the outer bright planes to surface termination sites mainly occupied by Cl while no significant signal of C occupied atomic planes is visible within the Ti_3C_2 structure in HAADF-STEM imaging. This interpretation is supported by local electron energy loss spectroscopy (EELS) mapping (Figure S9a–e, Supporting Information), which shows a significantly higher signal of Cl in between consecutive Ti_3C_2 layers. In contrast, only three bright layers can be observed in each N-containing $\text{Ti}_3\text{C}_2\text{T}_x$ layer (Figure 4f), similar to the reported $\text{HF-Ti}_3\text{CT}_x$,^[33] evidencing the successful substitution of Cl termination by a lighter element. Local STEM-EELS mapping (Figure S9f–j, Supporting Information) shows an alternation of N concentration in correlation with Ti_3C_2 layers, indicating that N is mainly located between Ti_3C_2 layers, on their surfaces, evidencing further the successful surface metathesis of $\text{Ti}_3\text{C}_2\text{T}_x$ from Cl to N.

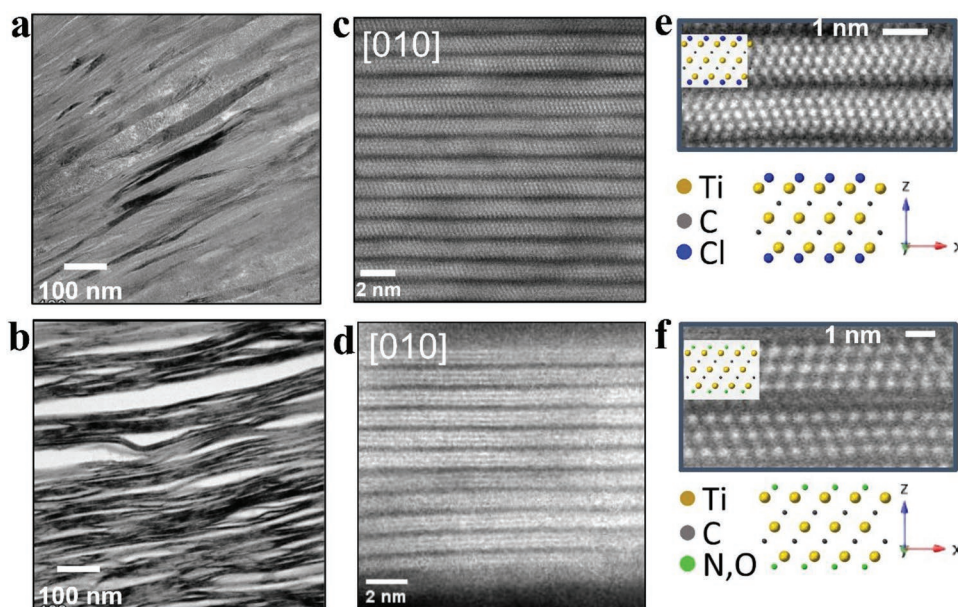


Figure 4. High-resolution transmission electron microscopy images at a scale of a) Cl-containing and b) N-containing $\text{Ti}_3\text{C}_2\text{Cl}_x$ a 100 nm. Atomic resolution high-angle annular dark-field (HAADF) images of c) Cl-containing and d) N-containing $\text{Ti}_3\text{C}_2\text{Cl}_x$ at a scale of 2 nm. HAADF images of e) Cl-containing and f) N-containing $\text{Ti}_3\text{C}_2\text{Cl}_x$ sample at a scale of 1 nm.

Overall, the post-thermal nitrification turns out to only modify the surface termination groups of the pristine MXene while maintaining the Ti_3C_2 -skeleton.

This surface termination exchange approach also offers great opportunities to tune the surface chemistry of MXene by using various molten salts based on other anions (such as HS^- , NH_4^+ , S^{2-} , Se^{2-} , Te^{2-} , or P^{3-}). Figure S10, Supporting Information, shows examples of the successful modification from Cl- to S-terminated $\text{Ti}_3\text{C}_2\text{T}_x$ when using Li_2S as molten salt during post-thermal treatment as evidenced by EDS analysis, which avoids the generation of insoluble impurities when directly using S-contained Lewis acidic molten salt such as CuS (Figure S10, Supporting Information). By careful selection of the molten salt, the present surface termination exchange route offers possibilities to enrich the variety of surface termination of MXenes which are difficult to be directly prepared by previously reported Lewis acidic molten salt etching routes.^[15]

2.4. Electrochemical Characterizations

To evaluate the impact of surface modification on the electrochemical properties, $\text{Ti}_3\text{C}_2\text{T}_x$ powders were processed into free-standing electrode films by mixing 80 wt% of MXene powders together with 15 wt% of carbon black and 5 wt% of PTFE binder and tested in a 3 M H_2SO_4 aqueous electrolyte. Figure 5a shows cyclic voltammetry (CV) profiles collected at 20 mV s^{-1} of the $\text{Ti}_3\text{C}_2\text{T}_x$ before and after surface modifications. The electrochemical signature of the well-known HF- $\text{Ti}_3\text{C}_2\text{T}_x$ prepared from etching in LiF/HCl liquid electrolyte^[34] is also shown for comparison purpose (orange plot) as it shows to date the best electrochemical performance of MXene in aqueous electrolyte. CV of HF- $\text{Ti}_3\text{C}_2\text{T}_x$ ($\text{T} = \text{F}^-$, OH^-) is typical of a surface redox capacitive process,^[35] with a pair of broadened redox peaks

centered at $-0.72/-0.83$ V versus $\text{Hg}/\text{Hg}_2\text{SO}_4$, on top of a small capacitive rectangular box, as the result of the presence of F- and OH-termination groups. In comparison, pristine magnet-treated, namely $\text{Ti}_3\text{C}_2\text{Cl}_x$ (Figure S12, Supporting Information), and APS-treated samples, namely $\text{Ti}_3\text{C}_2\text{Cl}_x\text{O}_y$, (Figure 5a, black plot) show a poor electrochemical signature, with a set of redox peaks accounting for diffusion-limited processes together with a small capacity. The poor performance might be explained by the lack of $-\text{OH}$ surface group as revealed by the TPD-MS technique^[15] and its relatively hydrophobic surface observed from contact angle measurement.^[36] Indeed, it has been reported elsewhere the MXene electrochemical activity in aqueous-based electrolytes depends on the presence of water molecules in between the MXene layers.^[11] Thus, a hydrophilic MXene may be mandatory for good performance in aqueous electrolytes.

After post-thermal treatment in Li_3N , the electrochemical signature of the resulting N-containing $\text{Ti}_3\text{C}_2\text{T}_x$ shows a drastic improvement. A mirror-like CV with a capacitive rectangular box profile is obtained within a large potential range, together with one pair of sharp, minor redox peaks located at $-0.29/-0.34$ V versus $\text{Hg}/\text{Hg}_2\text{SO}_4$. Additionally, a set of broad peaks is visible at $-0.52/-0.65$ V versus ref., which could be associated with surface redox pseudocapacitive behavior, such as observed with N-doped porous carbons.^[37] On top of that, a large operating potential window of 1.0 V (from -1.1 to -0.1 V vs $\text{Hg}/\text{Hg}_2\text{SO}_4$) could be achieved with N-containing MXene, which is currently the maximum voltage window of MXene reported to date in 3 M H_2SO_4 .^[5] CVs were recorded at various scan rates ranging from 5 to 2000 mV s^{-1} (Figure 5b) and the similar CV shapes first confirm fast electrochemical kinetics. Table S5, Supporting Information, shows the capacity reaches 117 mAh g^{-1} (420 F g^{-1}) at 10 mV s^{-1} for a 100 s charge time (40 C rate) and 84 mAh g^{-1} (303 F g^{-1}) at 2000 mV s^{-1} for a 0.5 s charge time (8000 C rate). Figure S14a, Supporting Information,

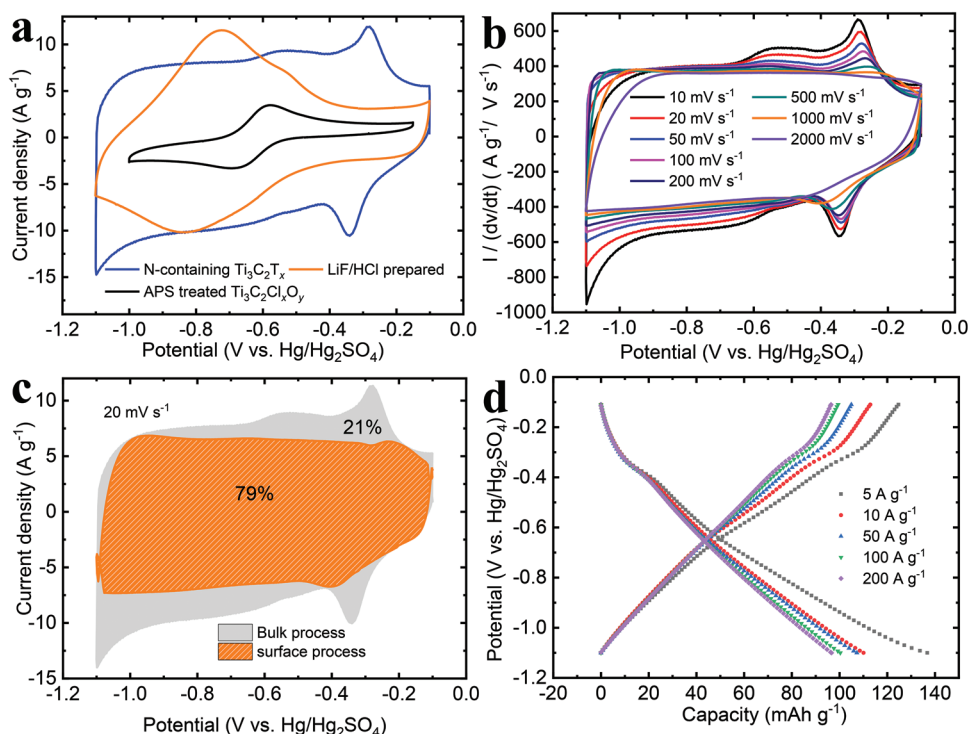


Figure 5. Influence of the surface functional groups on the electrochemical performance of $\text{Ti}_3\text{C}_2\text{T}_x$ in 3 M H_2SO_4 . The electrode weight loading was kept similar for all measurements at about 1 mg cm^{-2} . a) Comparison of the cyclic voltammetry data recorded at a potential scan rate of 20 mV s^{-1} of i) $\text{Ti}_3\text{C}_2\text{Cl}_x\text{O}_y$ MXene prepared by APS treatment ii) N-containing $\text{Ti}_3\text{C}_2\text{T}_x$ and iii) widely adopted $\text{Ti}_3\text{C}_2\text{T}_x$ ($T = \text{F}, \text{OH}$) prepared by LiF/HCl etched HF- $\text{Ti}_3\text{C}_2\text{T}_x$. Electrochemical characterization of N-containing $\text{Ti}_3\text{C}_2\text{T}_x$ in 3 M H_2SO_4 . b) Cyclic voltammetry profiles collected at scan rates from 10 to 2000 mV s^{-1} within a voltage window from -1.1 to -0.1 V ; c) Surface and bulk process contributions to the total charge at potential scan rates of 20 mV s^{-1} ; d) Galvanostatic charge/discharge curves profiles at current densities from 5.0 to 200.0 A g^{-1} versus capacity.

compares the power performance of pristine Cl-containing $\text{Ti}_3\text{C}_2\text{Cl}_x$, N-containing $\text{Ti}_3\text{C}_2\text{T}_x$ and conventional F- and OH-terminated HF- $\text{Ti}_3\text{C}_2\text{T}_x$. The N-containing $\text{Ti}_3\text{C}_2\text{T}_x$ achieves the highest capacitance and best power performance reported so far for any MXene electrode, to the best of our knowledge.^[5] To further emphasize the superiority of the N-containing MXene, the relevant literature has been summarized in Figure S14b, Supporting Information, together with Table S6, Supporting Information, which shows N-containing MXene has superior power capability compare to the state of the art with similar weight loading. These results also show that the electrochemical signature and performance are dominated by the surface terminations of MXene, and especially electron distribution toward the high surface area nanomaterials seems to be now seamless.

As previously mentioned, nitrogen groups are known to favor the pseudocapacitive contribution of nitrogen-doped carbon, which usually leads to an enhancement in the ion storage capability of N-doped carbon in supercapacitors.^[38–40] For example, the nitrogen-doped mesoporous carbon was reported to show an outstanding capacitance in $0.5 \text{ M H}_2\text{SO}_4$ electrolyte with a pronounced redox peak related to pyridinic and pyrrolic nitrogen groups.^[37] Just calculated from the sheer amount of nitrogen (at maximum one nitrogen for 182 mass units), this could work out, as protonation of all nitrides to $=\text{N}-\text{H}$ under simultaneous reduction of a Ti(IV) center to Ti(III) would account for 161 mAh g^{-1} .

To shed some light on the charge storage kinetics and pseudocapacitive activity from nitrogen groups of N-containing $\text{Ti}_3\text{C}_2\text{T}_x$, a kinetic analysis was further carried out first by plotting the peak current (i) of the redox process at $-0.29/-0.34 \text{ V}$ versus $\text{Hg}/\text{Hg}_2\text{SO}_4$ versus scan rate (v) from data collected in Figure S13, Supporting Information, in log scale (see Equation (3)):^[41]

$$i = av^b \quad (3)$$

A b -value of 1 indicates a surface-controlled process (no diffusion limitation), whereas 0.5 is characteristic of a diffusion-limited process (such as observed for bulk processes). As shown in Figure S15a, Supporting Information, the b -value was found to be 0.9 close to 1.0 for both cathodic and anodic peaks, evidencing a fast surface-like process. The influence of scan rate on the anodic and cathodic peak positions is shown in Figure S15b, Supporting Information, where E_p is the potential of the anodic and cathodic peak, $E_{1/2}$ is the average potential calculated by averaging the anodic and cathodic potentials at slow scan rates. The value of $E_p - E_{1/2}$ in the orange area remains almost constant, suggesting a highly reversible reaction for potential scan rates below 100 mV s^{-1} as expected for a surface redox controlled kinetics. Such high-rate capability is further supported by its large b value of 0.9. As the sweep rates increase to above 100 mV s^{-1} as indicated in the blue area, the peak separations increase, which can be mainly attributed to ohmic behavior. Moving further, the fitting method proposed by Dunn et al.^[42] was used to split the contribution of

diffusion-limited processes—bulk—from surface-controlled processes, using Equation (4):

$$i(v) = k_1 v + k_2 v^{1/2} \quad (4)$$

where k_1 (mA s V⁻¹) and k_2 (mA s^{1/2} V^{-1/2}) are two kinetic constants, i the current (mA) and v the potential scan rate (V s⁻¹). As shown in Figure 5c, non-diffusion limited surface-like redox processes account for about 79% of the total current at a scan rate of 20 mV s⁻¹, thus explaining the excellent kinetic and rate capability of the material.

Galvanostatic charge/discharge plots (Figure 5d; Figure S16, Supporting Information) confirm the unique electrochemical signature and impressive power performance of the electrode with a sloping voltage profile at different current densities from 5 A g⁻¹ to 200 A g⁻¹, as expected from the rectangular box-like CV shape displayed in Figure 5b. The Ti₃C₂T_x electrode capacity reaches 125 mAh g⁻¹ (corresponding to ≈75% from theoretical capacity^[5]) at 21 C rate and 97 mAh g⁻¹ at 1800 C rate (see Table S7, Supporting Information). Also cycling stability was more than impressive with 87% capacity retention after 20 000 cycles (Figure S17, Supporting Information). A specific capacity of 400 F g⁻¹ at 1 V for a mostly surface-controlled process is according to our knowledge near the best-in-class value for supercapacitors which can be underlined with a geometric model. 400 F g⁻¹ recalculate to 4.2 mmol g⁻¹ electrons and counterions per g, a very high value even for the adsorption of small, neutral gases (such as CO₂). Assuming delamination to single MXene sheets and dividing specific capacity by specific surface area, this again translates to about 2.45 × 10⁻⁵ moles m⁻² or 15 ions nm⁻², with some minor simplifications taken. This is close to the physically possible limit of tight packing onto a surface, the Langmuir monolayer. Nitrogen surface functionalization thereby has enabled to access the complete potential of the MXene in a highly reversible, high-rate performing way. It would be interesting to extend these measurements to higher voltage windows, as even higher voltages could not drive more ions to electro-adsorb in the current mode, that is, we expect the curve to bend down at higher voltages. This is then electric charge storage at the packing limit.

To get a better insight into the charge storage mechanism, an in-operando XRD study was performed on N-containing Ti₃C₂T_x-MXene in a 3 M H₂SO₄. Figure 6 shows the change of the (002) peak position during cycling, which is ascribed to the change of the interlayer spacing. Prior to the in situ XRD cycling, the (002) peak shifted after immersion in the 3 M H₂SO₄ electrolyte for 2 h as observed in Figure 6b, corresponding to an increase of 0.4 Å interlayer spacing and 0.8 Å increase of the c-lattice parameter, which is often attributed to H₂O intercalation as shown in previous reports.^[43] The contour map of in situ XRD patterns collected during anodic and cathodic scans for the first two cycles (Figure 6a) shows a reversible shift of the (002) peak. Figure 6c displays the change of the c-lattice parameter calculated based on the (002) peak positions of the first discharge and charge, showing that there are shrinkage and expansion of the c-lattice parameter during cycling. During the cathodic scan, the c-lattice parameter was found to be ≈26.3 Å at -0.1 V and it expanded quickly to 27.8 Å at -0.8 V versus Hg/Hg₂SO₄, then keeps slowly increasing to 28.0 Å from -0.8 to -1.0 V versus Hg/Hg₂SO₄. During the anodic scan, the c-lattice parameter remained almost constant from

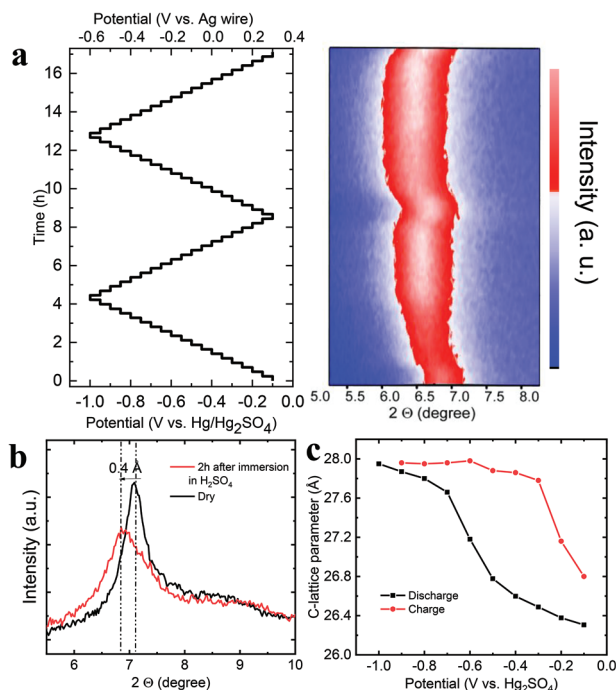


Figure 6. Electrochemical in situ X-ray diffraction study of the N-containing Ti₃C₂T_x in 3 M H₂SO₄. a) In situ XRD maps of the (002) peak during chronoamperometry scans with stepped potential and resulting current as a function of time for two different cycles. b) XRD patterns of N-containing Ti₃C₂T_x dry and immersed in 3 M H₂SO₄ for 2 h. c) Change of the c-lattice parameter with potential.

28.0 Å to 27.8 Å until -0.3 V, followed by an abrupt dropping again to 26.8 Å at -0.1 V versus Hg/Hg₂SO₄. Therefore, the maximum change of the c-lattice parameter is 1.6 Å during one cycle, which is larger than the 0.5 Å of the reported HF-MXene in 3 M H₂SO₄ aqueous electrolyte.^[44] The radius of a sulfate ion being 2.42 ± 0.07 Å,^[45] sulfate ions are not assumed to be involved in the intercalation (cathodic scan) and deintercalation (anodic scan) process, but the protons.^[11]

Moreover, the increased interlayer spacing change is consistent with the recent modeling study showing increased water molecules coming between the layers during proton intercalation for HF-MXene after nitrogen doping.^[46]

3. Conclusions

A molten salt synthesis route by selecting FeCl₂ as molten salt was used to prepare Cl-terminated Ti₃C₂T_x. To remove the Fe metal impurity, a mechanical magnet separation method has been adopted to get O-free halogen-terminated Ti₃C₂T_x. In a second step, a post-thermal treatment in molten salt with Li₃N was applied for surface termination substitution. Interestingly, the N-containing Ti₃C₂T_x owns surface redox behavior characterized by a unique mirror-like CV with a capacitive rectangular box profile together with one pair of sharp redox peaks in sulfuric acid electrolyte. It delivers a high gravimetric capacity of 117 mAh g⁻¹ (420 F g⁻¹ over 1.0 V voltage window) and 72% of the capacity remains even at 8000 C during 0.5 s discharge (charge), outperforming by far the widely adopted LiF/HCl

etched $\text{Ti}_3\text{C}_2\text{T}_x$ in aqueous electrolytes. It is interesting to compare the current data with the previous best-in-class supercapacitor materials, thin mesoporous crystalline metal oxide films as discussed by Dunn, Tolbert, and Brezesinski.^[47,48] We find in these papers similar maximal capacity values (also given by counterion packing), but highly deformed capacity–voltage curves already at much lower rates. In addition, such metal-oxide films only work when they are very thin (about 200 nm), while thicker films tend to show much lower performance, because of missing conductivity. The real progress of the presented system is not only in the battery-like high capacities, but in power density and loading rate, as well as in a voltage-independent capacity, all pointing to the advantages of a 2d-nano-system with a metal-like conductivity and electron transit paths at their surface. To conclude, this work thereby emphasizes the effectiveness of tuning the surface chemistry in MXene materials for improving electrochemical performance to the currently possible physical-chemical limit, thus accessing also the best possible supercapacitors.

4. Experimental Section

Preparation of Cl-Containing $\text{MS-Ti}_3\text{C}_2\text{T}_x$: Ti_3AlC_2 (400 mesh, purchased from Carbon-Ukraine Ltd.) was used as the MAX phase precursor, and FeCl_2 (Sigma-Aldrich, CAS # 7758-94-3) was selected as the main etching molten salt, while NaCl/KCl was used as the supporting electrolytes. In a typical procedure, the MAX phase was mixed with molten salt according to a specific ratio (e.g., $\text{Ti}_3\text{AlC}_2\text{:FeCl}_2\text{:NaCl/KCl} = 1\text{:}3\text{:}2\text{:}2$ in molar ratio) and ground well to obtain a homogenous distribution of particles. Then the mixture was heated for 7 h at 700 °C under the protection of argon (99.999%, ultra-high purity 5.0) flow. The as-synthesized products were washed with deionized water to remove the excess molten salt and further put in contact with a magnet to remove the Fe to achieve unitary Cl-terminated $\text{Ti}_3\text{C}_2\text{Cl}_x$. To replace part of Cl- with O-surface termination, the as-synthesized product was added inside the APS ($(\text{NH}_4)_2\text{S}_2\text{O}_8$, Sigma-Aldrich, CAS # 7727-54-0) solution to dissolve the residual Fe and the APS-treated $\text{Ti}_3\text{C}_2\text{Cl}_x\text{O}_y$ (0.1 M APS for 4 h). Then, the treated MXene was collected by centrifugation, followed by washing with a large amount of distilled water to remove the residual salts. All the powders were dried inside an oven at 80 °C. Note that the above process should be performed carefully to avoid the possible oxidation during the annealing since the O content of pristine MXene can affect the result of surface termination exchange.

Preparation of N-Containing $\text{MS-Ti}_3\text{C}_2\text{T}_x$: After drying, the magnet-treated $\text{Ti}_3\text{C}_2\text{Cl}_x$ was mixed with Li_3N (>99.5%, Sigma-Aldrich, CAS # 26134-62-3) together with LiCl and KCl as supporting electrolytes in the glove box since both LiCl and Li_3N can easily react with moisture to add extra O content. The precursor of N-containing $\text{Ti}_3\text{C}_2\text{T}_x$ was the mixture of $\text{Ti}_3\text{C}_2\text{Cl}_x\text{:Li}_3\text{N:LiCl:KCl} = 2\text{:}3\text{:}100\text{:}70$ in molar ratio. The mixtures were then transferred inside the Ar furnace and heated at 550 °C for 12 h. The product was washed with water and collected by vacuum filtration followed by drying inside an oven of 60 °C.

Preparation of LiF/HCl Etched HF- $\text{Ti}_3\text{C}_2\text{T}_x$: To prepare HF- $\text{Ti}_3\text{C}_2\text{T}_x$, the Ti_3AlC_2 MAX phase (400 mesh, purchased from Carbon-Ukraine Ltd.) was immersed in an etching solution of HCl and LiF, similar to previously reported.^[34] Specifically, 2 g of LiF (Fisher, 98.5%) was added into 40 mL of 9 M HCl (Fisher), followed by the slow addition of 2 g of Ti_3AlC_2 . The reaction was kept for 48 h at 35 °C water bath under the protection of N_2 gas and the obtained mixture was centrifugated and washed with deionized water until the supernatant reached a pH of 6. The suspension was kept under sonication for 1 h in an ice bath under N_2 for delamination, followed by a vacuum-filtering process for preparing the freestanding HF- $\text{Ti}_3\text{C}_2\text{T}_x$ electrode.

Physical Characterizations: X-ray diffraction (XRD) data were collected by a D4 X-ray diffractometer (Bruker, Germany) equipped with Cu K- α radiation ($\lambda = 0.154$ nm). The morphology of the MXenes was observed with a Scanning Electron Microscope (SEM) JSM 7100F (JEOL, Japan) with energy-dispersive X-ray spectroscopy (EDX) capabilities (Bruker, XFlash 6130). In situ high-temperature XRD was performed under an inert atmosphere (N_2 , 100 mL min⁻¹) with D8 X-ray diffractometer (Bruker, Germany) equipped with Cu K- α radiation ($\lambda = 0.154$ nm). The sample was placed in a ceramic cell and heat-treated up to 700 °C at a rate of 10 °C min⁻¹. The contact angle meter (DSA30 Drop Shape Analyzer from Kruss) was adopted to measure the water contact angle (WCA) of the $\text{Ti}_3\text{C}_2\text{T}_x$ MXene pellet, which was pressed by a pressing machine under 2 tons of pressure. Elemental analysis was performed with a vario MICRO cube CHNOS elemental analyzer (Elementar Analysensysteme GmbH, Langenselbold) and Spectrometer ICP-AES Horiba ULTIMA 2. Fourier-transform infrared spectroscopy (FTIR), in conjunction with attenuated total reflection (ATR), was used to record infrared spectra in a Thermo Scientific Nicolet model 6700 FT-IR spectrometer between 4000 and 400 cm⁻¹. Transmission electron microscopy (TEM) investigations were performed on a double Cs corrected JEOL JEM-ARM200F equipped with a cold-field emission gun and a Gatan Quantum GIF spectroscopy system. Samples were dispersed in ethanol and sonicated for ≈ 10 min. Dispersions were then drop-casted on lacey carbon Ni grids (MicroToNano) and dried prior insertion to the TEM. The TEM was operated at 200 kV and a probe convergence angle of 25 mrad was used for scanning (S)TEM operation. High-angle annular dark-field (HAADF-) STEM images were collected with an angular collection semi-angle range from 50 to 180 mrad. A dispersion of 0.25 eV per channel was used for electron energy loss spectroscopy. Data were treated using Gatan's Digital Micrograph (GMS3) version 3.4. In particular, HR-STEM images were filtered by applying a combined (default) soft rectangle and band pass filter. The Brunauer–Emmett–Teller (BET) equation was used to calculate the specific surface area (SSA), from the linear plot in the relative pressure range (P/P₀). The pore size distribution (PSD) was determined by the non-local density functional theory (NLDFT) standard model with SAIEUS software from Micromeritics. Nitrogen adsorption–desorption isotherms were measured at 77K using Micromeritics ASAP 2020.

Electrochemical Measurements: To prepare the electrodes, $\text{Ti}_3\text{C}_2\text{T}_x$ powders were mixed with PTFE binder and carbon black conducting additive (80 wt% of MXenes powders, 15 wt% of carbon black and 5 wt% of PTFE binder) and calendared into the film. After drying, MXene films were used as the working electrode to assemble three-electrode cells with YP50 as the counter and Hg/Hg₂SO₄ as the reference electrode. The mass loading was controlled at ≈ 1.0 mg cm⁻². Ti foils were selected as current collector, which allowed to extend the working potential window to 1 V (from -1.1 to -0.1 V vs Hg/Hg₂SO₄), such as reported in the early work.^[5] 3 M H₂SO₄ in water was used as the electrolyte, while two layers of 260 μm -thick porous borosilicate glass fibers (Whatman GF/B) were used as the separator. Cyclic voltammetry, impedance and galvanostatic cycling were performed using a VMP3 potentiostat (Biologic, France).

For the in-operando XRD test, the specially made Swagelok cells were assembled in air, using N-containing $\text{Ti}_3\text{C}_2\text{T}_x$ MXene as the working electrode deposited onto titanium disk as the current collector, and YP50 as the counter electrode. Before adding the MXene working electrode, a SpectroMembrane was placed onto the bottom part of the Swagelok cell to avoid electrolyte leakage. The in situ XRD cell was connected to a Biologic potentiostat to conduct the electrochemical cycling at chronoamperometry experiments with a stepped potential of 0.05 V within a potential range of 0.9 V. The XRD patterns were recorded in-operando during the galvanostatic test (a total of 16 min for one full pattern).

Calculations for the Electrochemical Tests: The capacitance of the electrode could be calculated from the CV by the following equation:

$$C = \frac{\int_0^i dt}{\Delta E} \quad (5)$$

where i is the current (A) and ΔE is the potential window (V).

The specific capacity was calculated according to the equation:

$$Q = \frac{I \times \Delta t}{m} \quad (6)$$

where Q is gravimetric capacity (mAh g⁻¹), I is the current applied (A), Δt is the discharge time (h), and m is the mass (kg).

Supporting Information

Supporting Information is available from the Wiley Online Library or from the author.

Acknowledgements

L.L. was supported by ERC Synergy Grant MoMa-Stor#951513. P.S. and P.L.T. acknowledge the support from Agence Nationale de la Recherche (Labex Store-ex) and ERC Synergy Grant MoMa-Stor #951513. The authors would like to thank Antje Völkel and Christelle Chiron for help with elemental analysis.

Open access funding enabled and organized by Projekt DEAL.

Conflict of Interest

The authors declare no conflict of interest.

Data Availability Statement

The data that support the findings of this study are available from the corresponding author upon reasonable request.

Keywords

molten salts approach, pseudocapacitance, supercapacitors, surface termination, Ti₃C₂T_x MXene

Received: August 8, 2022

Revised: October 27, 2022

Published online: November 23, 2022

- [1] M. R. Lukatskaya, O. Mashtalir, C. E. Ren, Y. Dall'Agnese, P. Rozier, P. L. Taberna, M. Naguib, P. Simon, M. W. Barsoum, Y. Gogotsi, *Science* **2013**, 341, 1502.
- [2] M. Naguib, M. Kurtoglu, V. Presser, J. Lu, J. Niu, M. Heon, L. Hultman, Y. Gogotsi, M. W. Barsoum, *Adv. Mater.* **2011**, 23, 4248.
- [3] B. Anasori, M. R. Lukatskaya, Y. Gogotsi, *Nat. Rev. Mater.* **2017**, 2, 16098.
- [4] M. Ghidui, M. R. Lukatskaya, M.-Q. Zhao, Y. Gogotsi, M. W. Barsoum, *Nature* **2014**, 516, 78.
- [5] M. R. Lukatskaya, S. Kota, Z. Lin, M.-Q. Zhao, N. Shpigeli, M. D. Levi, J. Halim, P.-L. Taberna, M. W. Barsoum, P. Simon, *Nat. Energy* **2017**, 2, 17105.
- [6] L. Liu, P.-L. Taberna, B. Dunn, P. Simon, *ACS Energy Lett.* **2021**, 6, 4311.
- [7] Q. Tang, Z. Zhou, P. Shen, *J. Am. Chem. Soc.* **2012**, 134, 16909.
- [8] Y. Xie, M. Naguib, V. N. Mochalin, M. W. Barsoum, Y. Gogotsi, X. Yu, K.-W. Nam, X.-Q. Yang, A. I. Kolesnikov, P. R. Kent, *J. Am. Chem. Soc.* **2014**, 136, 6385.
- [9] G. R. Berdiyorov, K. A. Mahmoud, *Appl. Surf. Sci.* **2017**, 416, 725.
- [10] D. Li, X. Chen, P. Xiang, H. Du, B. Xiao, *Appl. Surf. Sci.* **2020**, 501, 144221.
- [11] H. Shao, K. Xu, Y.-C. Wu, A. Iadecola, L. Liu, H. Ma, L. Qu, E. Raymundo-Piñero, J. Zhu, Z. Lin, *ACS Energy Lett.* **2020**, 5, 2873.
- [12] L. Liu, M. Orbay, S. Luo, S. Duluard, H. Shao, J. Harmel, P. Rozier, P.-L. Taberna, P. Simon, *ACS Nano* **2022**, 16, 111.
- [13] Y. Dall'Agnese, M. R. Lukatskaya, K. M. Cook, P.-L. Taberna, Y. Gogotsi, P. Simon, *Electrochem. Commun.* **2014**, 48, 118.
- [14] M. Li, J. Lu, K. Luo, Y. Li, K. Chang, K. Chen, J. Zhou, J. Rosen, L. Hultman, P. Eklund, *J. Am. Chem. Soc.* **2019**, 141, 4730.
- [15] Y. Li, H. Shao, Z. Lin, J. Lu, L. Liu, B. Duployer, P. O. Persson, P. Eklund, L. Hultman, M. Li, *Nat. Mater.* **2020**, 19, 894.
- [16] Y. Bai, C. Liu, T. Chen, W. Li, S. Zheng, Y. Pi, Y. Luo, H. Pang, *Angew. Chem.* **2021**, 133, 25522.
- [17] V. Kamysbayev, A. S. Filatov, H. Hu, X. Rui, F. Lagunas, D. Wang, R. F. Klie, D. V. Talapin, *Science* **2020**, 369, 979.
- [18] Y.-R. Luo, *Comprehensive Handbook of Chemical Bond Energies*, CRC Press, Boca Raton, FL **2007**.
- [19] J. Liu, Z. Liu, H. B. Zhang, W. Chen, Z. Zhao, Q. W. Wang, Z. Z. Yu, *Adv. Electron. Mater.* **2020**, 6, 1901094.
- [20] J. Lu, I. Persson, H. Lind, J. Palisaitis, M. Li, Y. Li, K. Chen, J. Zhou, S. Du, Z. Chai, *Nanoscale Adv.* **2019**, 1, 3680.
- [21] T. Ichikawa, S. Isobe, N. Hanada, H. Fujii, *J. Alloys Compd.* **2004**, 365, 271.
- [22] P. Larkin, *Infrared and Raman Spectroscopy: Principles and Spectral Interpretation*, Elsevier, Amsterdam **2017**.
- [23] K. T. Sarang, X. Zhao, D. Holta, M. Radovic, M. J. Green, E.-S. Oh, J. L. Lutkenhaus, *Nanoscale* **2020**, 12, 20699.
- [24] S. A. Rounaghi, D. E. Vanpoucke, H. Eshghi, S. Scudino, E. Esmaeili, S. Oswald, J. Eckert, *Phys. Chem. Chem. Phys.* **2017**, 19, 12414.
- [25] A. Djire, H. Zhang, J. Liu, E. M. Miller, N. R. Neale, *ACS Appl. Mater. Interfaces* **2019**, 11, 11812.
- [26] X. Cao, C. Liu, Y. Hu, W. Yang, J. Chen, *J. Nanomater.* **2016**, 2016, 1.
- [27] A. Prakash, S. D. Nehate, K. B. Sundaram, *Opt. Lett.* **2016**, 41, 4249.
- [28] D. Magne, V. Mauchamp, S. Célérier, P. Chartier, T. Cabioc'h, *Phys. Chem. Chem. Phys.* **2016**, 18, 30946.
- [29] M. Zhang, R. Liang, N. Yang, R. Gao, Y. Zheng, Y. P. Deng, Y. Hu, A. Yu, Z. Chen, *Adv. Energy Mater.* **2022**, 12, 2102493.
- [30] J. Zhu, Y. Tang, C. Yang, F. Wang, M. Cao, *J. Electrochem. Soc.* **2016**, 163, A785.
- [31] P. Hartel, H. Rose, C. Dinges, *Ultramicroscopy* **1996**, 63, 93.
- [32] B. Rafferty, D. Nellist, J. Pennycook, *Microscopy* **2001**, 50, 227.
- [33] X. Wang, X. Shen, Y. Gao, Z. Wang, R. Yu, L. Chen, *J. Am. Chem. Soc.* **2015**, 137, 2715.
- [34] M. Alhabeb, K. Maleski, B. Anasori, P. Lelyukh, L. Clark, S. Sin, Y. Gogotsi, *Chem. Mater.* **2017**, 29, 7633.
- [35] P. Simon, Y. Gogotsi, *Nat. Mater.* **2020**, 19, 1151.
- [36] L. Liu, M. Orbay, S. Luo, S. Duluard, H. Shao, J. Harmel, P. Rozier, P.-L. Taberna, P. Simon, *ACS Nano* **2021**, 16, 111.
- [37] T. Lin, I.-W. Chen, F. Liu, C. Yang, H. Bi, F. Xu, F. Huang, *Science* **2015**, 350, 1508.
- [38] D. Yang, Y. Song, Y.-J. Ye, M. Zhang, X. Sun, X.-X. Liu, *J. Mater. Chem. A* **2019**, 7, 12086.
- [39] O. Ornelas, J. M. Sieben, R. Ruiz-Rosas, E. Morallon, D. Cazorla-Amorós, J. Geng, N. Soin, E. Siores, B. F. Johnson, *Chem. Commun.* **2014**, 50, 11343.
- [40] P. Treeweranuwat, P. Boonyoung, M. Chareonpanich, K. Nueangnoraj, *ACS Omega* **2020**, 5, 1911.
- [41] H. Lindström, S. Södergren, A. Solbrand, H. Rensmo, J. Hjelm, A. Hagfeldt, S.-E. Lindquist, *J. Phys. Chem. B* **1997**, 101, 7717.
- [42] J. Wang, J. Polleux, J. Lim, B. Dunn, *J. Phys. Chem. C* **2007**, 111, 14925.
- [43] M. Ghidui, J. Halim, S. Kota, D. Bish, Y. Gogotsi, M. W. Barsoum, *Chem. Mater.* **2016**, 28, 3507.

- [44] X. Mu, D. Wang, F. Du, G. Chen, C. Wang, Y. Wei, Y. Gogotsi, Y. Gao, Y. Dall'Agnese, *Adv. Funct. Mater.* **2019**, 29, 1902953.
- [45] Y. Marcus, *Chem. Rev.* **1988**, 88, 1475.
- [46] H. Li, K. Xu, P. Chen, Y. Yuan, Y. Qiu, L. Wang, L. Zhu, X. Wang, G. Cai, L. Zheng, *Natl. Sci. Rev.* **2022**, 9, nwac079.
- [47] T. Brezesinski, J. Wang, S. H. Tolbert, B. Dunn, *J. Sol-Gel Sci. Technol.* **2011**, 57, 330.
- [48] K. Brezesinski, J. Wang, J. Haetge, C. Reitz, S. O. Steinmueller, S. H. Tolbert, B. M. Smarsly, B. Dunn, T. Brezesinski, *J. Am. Chem. Soc.* **2010**, 132, 6982.